Reconciling equatorward migration of Southern Ocean fronts with minor ice volume change during Miocene cooling

Suning Hou (s.hou@uu.nl)
Utrecht University https://orcid.org/0000-0002-8902-6367
Lennert Stap
AWI https://orcid.org/0000-0002-2108-3533
Ryan Paul
Utrecht University
Mei Nelissen
NIOZ Royal Netherlands Institute of Sea Research
Frida Hoem
Utrecht University https://orcid.org/0000-0002-8834-6799
Martin Ziegler
Faculty of Geosciences, Utrecht University https://orcid.org/0000-0003-3198-6434
Appy Sluijs
Utrecht University https://orcid.org/0000-0003-2382-0215
Francesca Sangiorgi
Utrecht University https://orcid.org/0000-0003-4233-6154
Peter Bijl
Faculty of Geosciences, Utrecht University https://orcid.org/0000-0002-1710-4012

Article

Keywords:

Posted Date: July 27th, 2023

DOI: https://doi.org/10.21203/rs.3.rs-3184669/v1

Additional Declarations: There is **NO** Competing Interest.

Reconciling equatorward migration of Southern Ocean fronts with minor Antarctic ice volume change during Miocene cooling

Suning Hou[1]*, Lennert B. Stap[2], Ryan Paul[1], Mei Nelissen[3], Frida S. Hoem[1], Martin Ziegler[1], Appy Sluijs[1], Francesca Sangiorgi[1], Peter K. Bijl[1]

[1]Department of Earth Sciences, Utrecht University, the Netherlands
[2]Institute for Marine and Atmospheric research Utrecht, Utrecht University, the Netherlands
[3]NIOZ Royal Netherlands Institute of Sea Research, Texel, The Netherlands

Abstract:

A Miocene phase of gradual climate cooling and CO_2 decline was recently shown not to be associated with major ice volume expansion, challenging a fundamental paradigm in the functioning of the Antarctic cryosphere. Here, we explore Miocene ice-ocean-climate interactions by presenting a multi-proxy reconstruction of subtropical front (STF) migration, bottom water temperature (BWT) and global ice volume change, using dinoflagellate cyst biogeography, benthic foraminiferal clumped isotopes, and sea surface temperature (SST) reconstructions from offshore Tasmania. We demonstrate a mid-late Miocene (16–9 Ma) equatorward migration (from ~53°S to ~42°S) and strengthening of the STF, concurrent with SST decline. We expand evidence for strong BWT decline and apparent absence of ice volume change into the late Miocene with new clumped isotope data. To reconcile these counterintuitive findings, we argue based on new, idealized ice sheet model simulations that the Miocene Antarctic ice sheet progressively lowered in height while expanding seawards during the mid-Miocene, to maintain a stable volume. This can only be achieved with rigorous intervention in model precipitation regimes and ice-ocean interactions and requires rethinking the interactions between ice-ocean and climate during Neogene cooling.

Introduction

Temperature contrasts between the equator and high latitudes are mitigated through poleward atmospheric and ocean heat transport[1,2]. Variability in the latitudinal sea surface temperature (SST) gradient is mostly a function of polar temperatures, which are much more variable than those at low latitudes because of polar amplification[3]. In turn, polar SSTs, especially offshore Antarctica, vary with prevailing cryosphere conditions, including sea ice extent[4,5]. The steepest part of the latitudinal SST gradient is at mid-latitudes, at the boundary between subtropical gyres and subpolar waters. On the Southern Hemisphere, this is the subtropical front (STF): the northern limit of the Southern

Ocean and the Antarctic Circumpolar Current (ACC), and the center of ocean carbon uptake[6] (Fig. 1). The ACC and associated oceanographic fronts, driven by westerlies and bathymetry[7], regulate deep ocean ventilation[8–10] and heat exchange between low and high latitudes[11,12]. In turn, the latitudinal position of westerlies is influenced by the extent of sea ice around Antarctica[13,14]. Oceanographic conditions around the ocean fronts thus play a central role in the latitudinal distribution of heat on the Southern Hemisphere, including the heat source that causes basal melt and instability of marine-terminating Antarctic ice sheets[6]. Future projections of polar climate change, and the consequences for cryosphere melt and sea level are highly uncertain[15], because changes in and interactions between Antarctic ice sheets, sea ice and oceanography bear numerous poorly constrained, non-linear feedbacks[6,16]. Important constraints on the functioning of this system in a warming world might come from reconstructions of geologic episodes during which the partial pressure of atmospheric CO_2 (pCO_2) was as high as projected for the future.

Throughout the Neogene (23–2.58 Ma), pCO_2 declined from 800 to 300 ppmv[17], global temperatures dropped[18,19], latitudinal SST gradients increased[20] and global ice volume[19,21–23] and sea ice expanded[24]. The current paradigm assigns pCO_2 decline as the primary driver, which, through polar amplification of cooling, stimulates ice growth and cooling in the regions of deep-water formation[18,25,26]. Yet, recent data have challenged this view. A recent study found that Neogene SST gradients increased in the subtropical gyre but decreased from the subtropical front to polar waters[27]. With relatively stable equatorial[28,29] and polar SSTs[30], this indicates that the mid-latitudes, rather than the high-latitudes[27], cooled most profoundly in the Neogene. Antarctic-proximal records suggest a retreated Antarctic ice sheet and warm Antarctic-proximal conditions[24,30,31] during the mid-Miocene Climatic Optimum (MCO) and profound seaward ice sheet advance during subsequent cooling termed the Middle Miocene Climatic Transition (MMCT)[21,23,32–34], in line with pCO_2 estimates[35]. Along with a rise in deep ocean benthic foraminifera oxygen isotope ratios ($\delta^{18}O_{bf}$), this suggests a strong increase in global ice volume. Yet, the first series of clumped isotope measurements (Δ_{47}, which deconvolves temperature and ice volume components in $\delta^{18}O_{bf}$ records) on Miocene benthic foraminifera[36–38] suggest higher-than-previously-estimated Bottom Water Temperatures (BWTs) during the MCO, and as a result, large global ice volume. These records also indicate strong BWT cooling during the MMCT, explaining most if not all of the $\delta^{18}O_{bf}$ rise, and therefore little to no ice volume buildup. However, the uncertainties in clumped isotope data and the limited resolution and temporal range of the records leave ambiguity on the true amount of BWT dropping and ice volume buildup during the mid-Miocene.

Like the modern, changes in the Southern Ocean, notably regarding fronts and currents, were likely vital for heat transport towards the ice sheet in the Neogene. A relatively weak ACC, initiated during the Eocene[39], intensified in the late Oligocene ~26 Ma[40] but modern-like strengths only developed in the late Neogene[41]. The development and latitudinal position of the fronts associated to the ACC are, however, still poorly constrained. To shed light on the links between (Antarctic) ice volume and dynamics, Southern Ocean oceanography and latitudinal SST gradients, we present a detailed reconstruction of Neogene STF migration history and surface and bottom water temperature offshore Tasmania, and pair these with new estimates of Antarctic ice volume change from the MCO across the MMCT. We use dinoflagellate cyst (dinocyst) biogeography[42] to reconstruct the position of Southern Ocean currents and fronts and combine these with published SST reconstructions. Finally, from benthic foraminiferal Δ_{47}, we assess deep-water temperature changes at the subtropical front, as well as sea water $\delta^{18}O$ ($\delta^{18}O_{sw}$) as a proxy for Antarctic ice change.

We demonstrate that there is a strengthening and equatorward migration of the STF from ~53° to ~42° between ~14 Ma and 7 MA, concurrent with progressive sea surface and bottom water cooling. The deep ocean cooling can completely explain benthic foraminifer $\delta^{18}O$ evolution, implying stable global ice volume. After 7 Ma, the northward shift of the STF is limited by the Australian continent, even though the SSTs continue to decrease. To reconcile expansion of subpolar ocean conditions and progressive Neogene Southern Ocean cooling with stable ice volume and compelling evidence of ice advance, we argue that the Miocene Antarctic ice sheet progressively lowered in height while expanding seawards during the mid-Miocene. We present idealized ice sheet model simulations that physically constrain this hypothesis. This changed geometry induced strong regional oceanographic responses with expansion of sea ice, cooling of the region of bottom-water formation and northwards migration of ocean fronts.

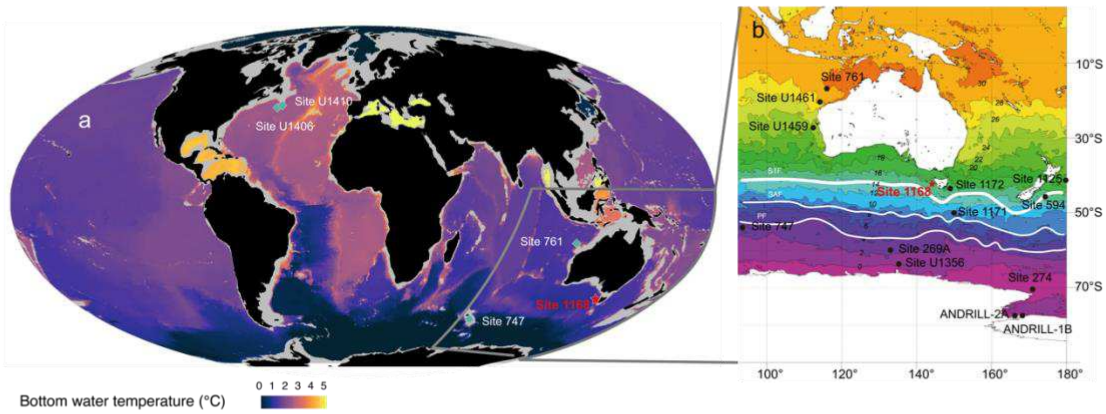

Figure 1: a. Global ocean bottom (>2500m) water temperature, in blue diamonds the sites from which Miocene clumped isotope data has been generated[36–38], modified from ref[43]. White line indicates the area of Fig 1b. b. Map of the Southern Ocean Sites with modern sea surface temperature and frontal systems positions[44]. STF=subtropical front; SAF=subantarctic front; PF=polar front.

Results

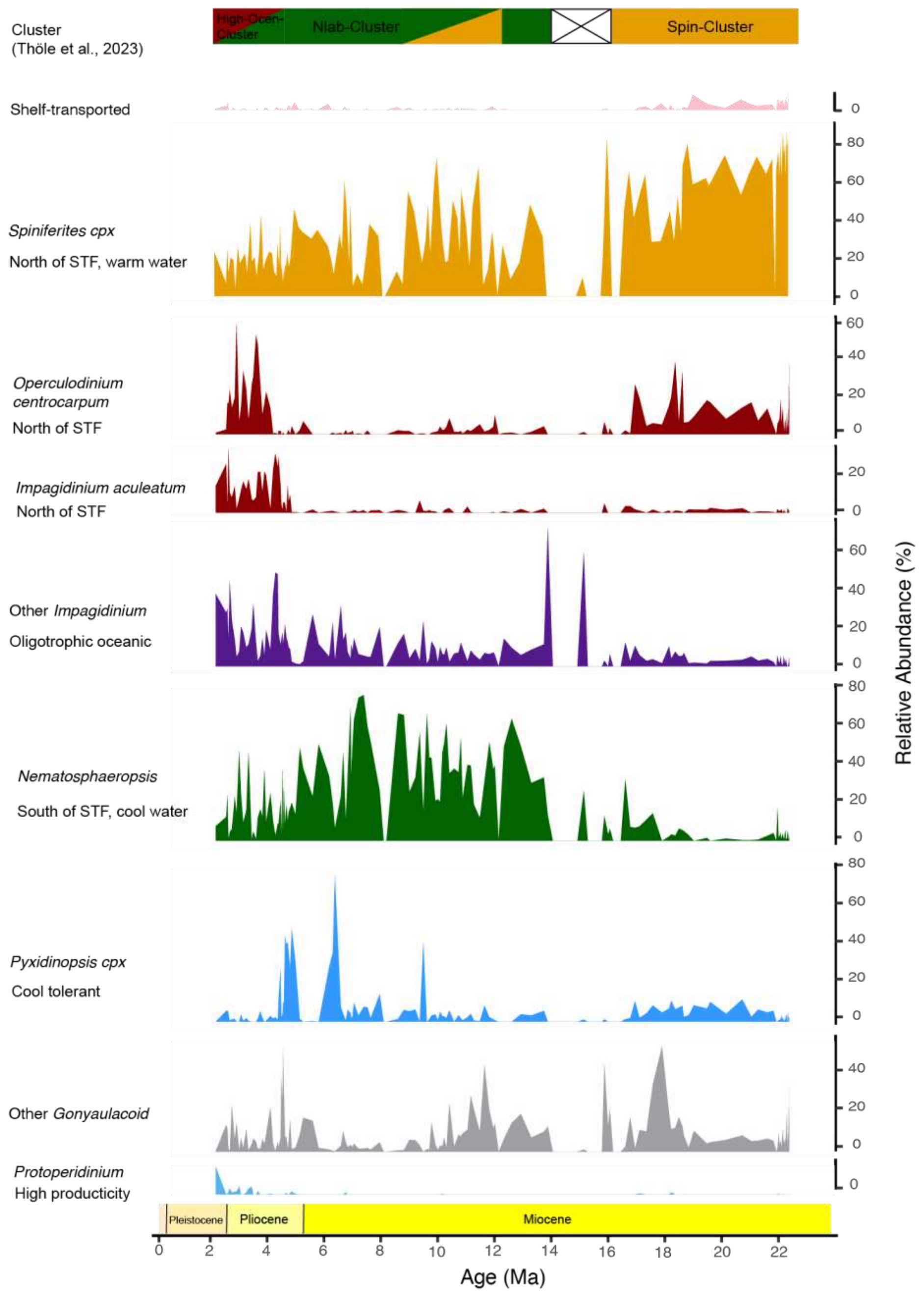

Figure 2: Dinoflagellate cyst assemblage results from ODP Site 1168, grouped by their ecological affinities based on ref[42] (see Table S1). Dinocysts are ordered from their known occurrence in in latitude from north (bottom) to south, with uncertain groups and heterotrophic species to the top.

Dinoflagellate-based surface oceanographic reconstruction of the subtropical front

The vast majority of the dinocysts encountered in the Neogene sediments from ODP Site 1168 are extant species of the modern Southern Ocean. The use of inferences from modern biogeographic distributions and affinities of dinocyst assemblage clusters[42] (see methods) hence allows reliable reconstructions of paleoceanographic conditions.

In early Miocene sediments at Site 1168, dinocyst assemblages are dominated by warm/temperate *Spiniferites* spp. (Fig. 2). This assemblage resembles the Spin cluster of ref[42], which now mainly thrives along the northwest coast of Australia and in low latitudes in the eastern Indian Ocean[42]. This cluster is associated with a modern SST of ~29±0.5°C, a temperature in line with that derived from biomarkers[27,42] (Fig. 5a). Early Miocene SSTs at Site 1168 were ~13 °C warmer than today, in spite of a ~10 ° more poleward position of the site[45]. Given these SSTs and dinocyst assemblages, we infer a strong influence of the Leeuwin Current, delivering heat and sustaining low-latitude dinoflagellate assemblages from western Australia towards the site. It implies that the STF was located to the south of the site. Gradual increases of *Operculodinium* spp. in this interval suggests gradually cooler-water influence, with an approaching STF from the south. We find occasional northward migrations of the STF (e.g., at ~22 Ma) in sporadic abundance of *N. labyrinthus,* concomitant to SST cooling (Fig. 5a).

Dinocysts are poorly preserved in MCO sediments (Fig. 2), and GDGT concentrations are low[27], pointing to enhanced sediment oxidation. The available palynological data for the MCO shows that the Spin cluster was replaced by *Impagidinium paradoxum* and *I. patulum*, which in the modern are restricted to temperate to equatorial open ocean regions between sub-tropical and subpolar systems[42]. Although it is unclear how this dinocyst assemblage differs from the Spin cluster in terms of ocean temperature, the biomarker-based SSTs indicate continued warmth during the MCO at the site (Fig. 5a). In any case, Site 1168 remained north of the STF.

The mid Miocene Climatic Transition (MMCT, ~14.5 to 12 Ma) marks the first interval of prevailing *N. labyrinthus* (Fig. 2). This species (Nlab cluster in ref[42]) is found most abundant in sediments south of the STF, in the modern subantarctic zone. We interpret the proliferation of Nlab and a progressive cooling towards subantarctic zone-like conditions (Fig. 5a) as a northward migration of the STF. At MMCT, the STF reached a similar position relative to that of Australia as during the last glacial maximum[46–48] (Fig. 4). Subsequent high-amplitude, short-term fluctuations of dinocyst assemblages between the Nlab and Spin cluster, and, albeit less pronounced, SST (Fig. 5), indicate strong (SSTs between 29°C and 11°C; Fig. 5a) variability of the latitudinal position of the STF until 7 Ma (Fig. 2).

From ~7 Ma, *N. labyrinthus* started to decrease in abundance. The Nlab-Cluster and the slightly warmer high-Ocen-Cluster alternate in the Pliocene (5–2 Ma) on orbital timescales, which is close to the modern assemblage, and bracket the modern STF[42] (SSTs between 25 °C and 10 °C; Fig. 5a). We interpret a southward migration of the frontal systems from the decline in Nlab and the return of high-Ocen cluster. Apparently, this continued cooling is not related to continued shifts of ocean frontal systems, but a cooling of the STF itself.

Overall, we deduce long-term cooling from the dinocyst assemblages, despite the ~8 degrees northward tectonic movement of the site during the Neogene. There was strong variability over glacial-interglacial climate fluctuations. The STF moved gradually northwards from 22–7 Ma (Fig. 3a–c). We infer a concomitant strengthening of the STF from steepened latitudinal SST gradient among mid latitudes[27], and from the fact that the STF was progressively pushed towards the southern margin of the Australian continent. From 7–5 Ma, the STF moved south from the site again, likely because of Australia's continued northward drift. This allowed for the return of influence of the warm Leeuwin Current at the Site (Fig. 3c, d).

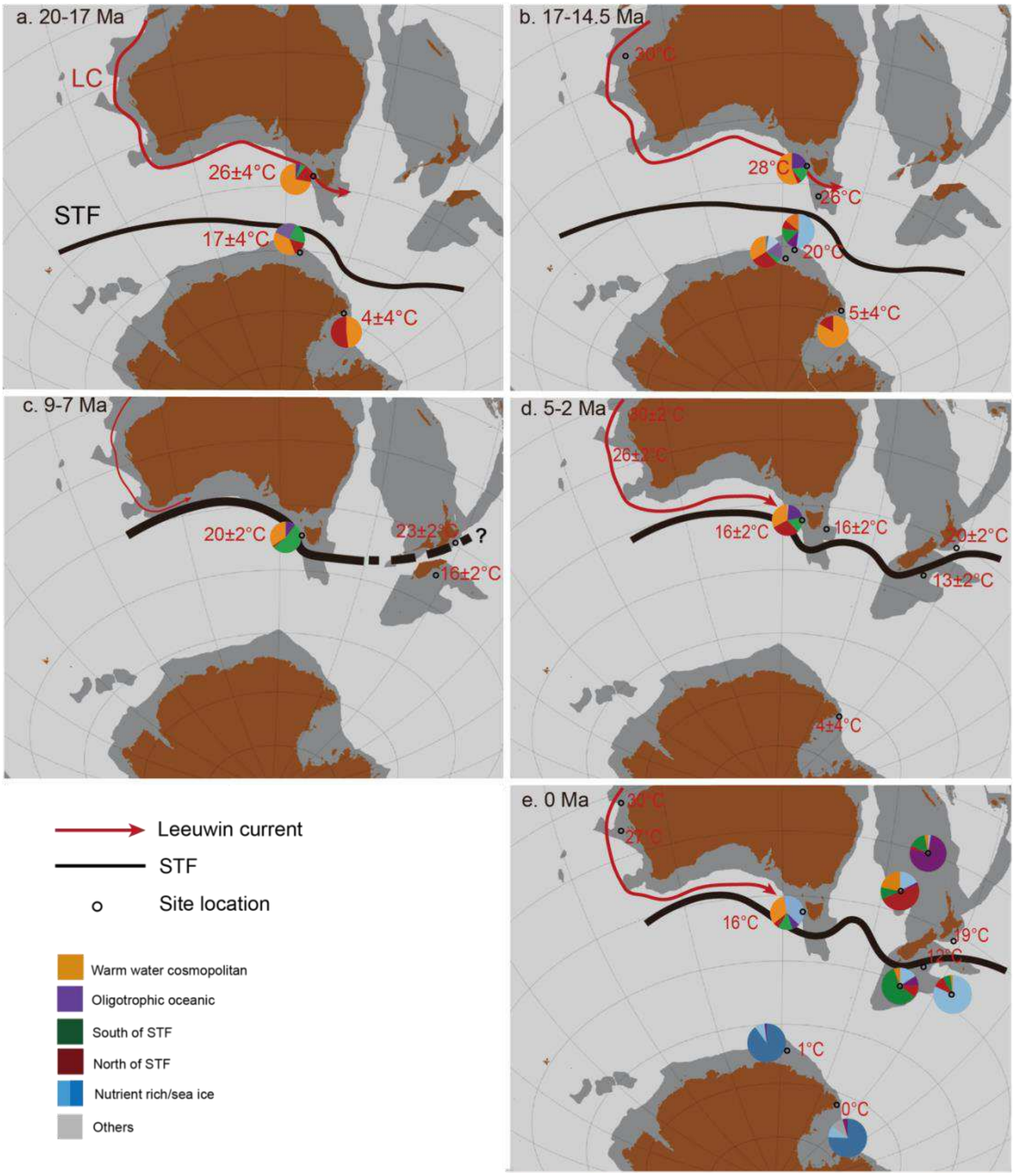

Figure 3: Subtropical Front migration history in the southeast Indian and southwest Pacific Ocean in 5 time slices from the start of the Neogene. (a) early Miocene 20-17 Ma, (b) MCO, 17-14.5 Ma (c) 9-7 Ma (d) 5-2 Ma (e) modern, 0 Ma. Average dinocyst assemblages for these time slices at Site 1168 are presented along with those from Site U1356[24], Site 269A[49], Site 274[40] and ANDRILL-2A[50]. The present-day dinocyst distribution is based on Thöle et al.[42]. Red arrow indicates the Leeuwin Current. Average SST for time slices at Site 1168 are presented along with those from U1356[24], Site 1172[51] , Site 1125[20], Site 594[20] and Ross Sea sites[30]. Solid black line indicates the STF, whereby the thickness of the line denotes the relative strength of the STF. Paleogeographic position of the continents and sites are generated with GPlates[52,53]. Dark brown areas indicate present-day landmass, dark grey indicates continental crust.

Benthic foraminiferal stable isotope ratios, Δ_{47} and sea water $\delta^{18}O$

The $\delta^{18}O_{bf}$ and $\delta^{13}C_{bf}$ records generally follow trends recorded at other Southern Ocean sites[36,37] (Fig. 4), including a 1‰ negative offset in $\delta^{18}O$ compared to the CENOGRID compilation[18]. At ~10 Ma, $\delta^{18}O_{bf}$ gradually increases from 1.5‰ (MCO) to 2.5‰, followed by a further rise to ~2.8‰ at the end of the Miocene (~5.3 Ma). Remarkably, we do not record pronounced steps across the MMCT as seen in other records[54]. The pronounced $\delta^{13}C_{bf}$ maxima (at 17 Ma) likely reflects the Monterey carbon isotope excursion[55–57] and values are in line with those in other records.

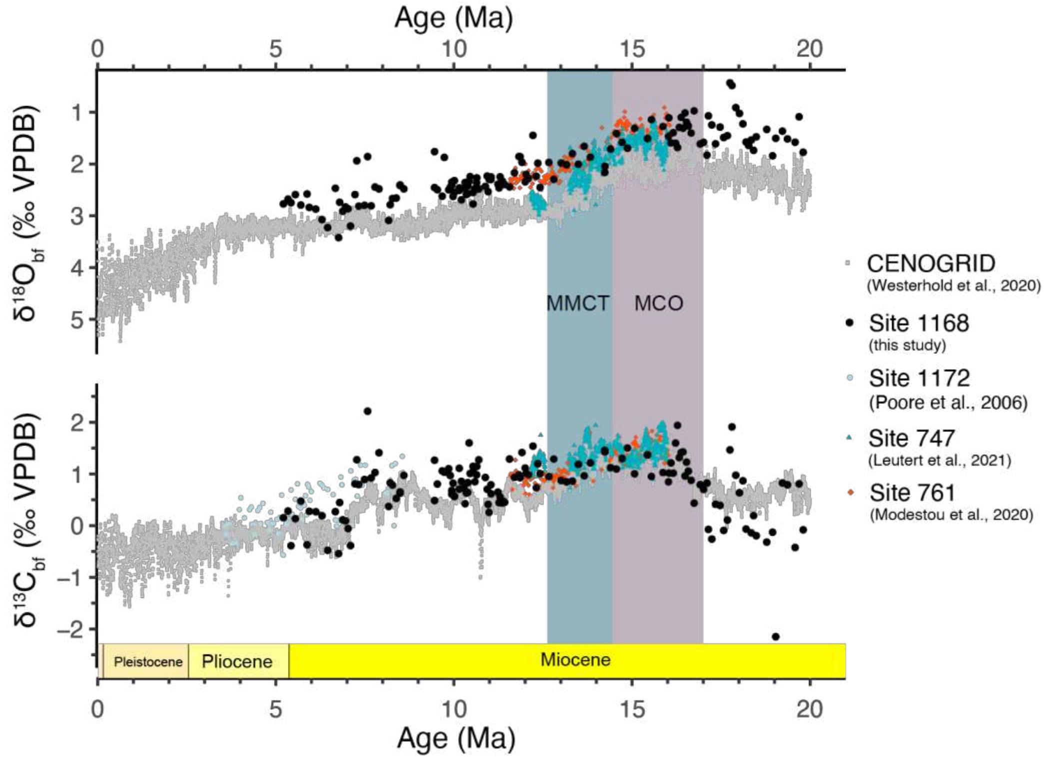

Figure 4. Benthic foraminiferal oxygen and carbon stable isotopes of Site 1168 (black dots) together with data from Site 1172[58] (blue dots), Site 747[37] (green triangles), Site 761[36] (red diamonds) and the CENOGRID stack[18] (grey dots). MCO = Mid-Miocene Climatic Optimum, MMCT = mid-Miocene Climatic Transition.

The benthic foraminiferal clumped isotope data from site 1168 fill critical mid- and late Miocene gaps in existing BWT compilations[38] and thus BWT and Antarctic ice dynamics (Fig. 5b). BWT, based on Δ_{47} data in ~1 Myr bins, at Site 1168 decreased gradually from 9.9±4.0°C (95% confidence interval) in the MCO (17–14.5 Ma) to 5.0±2.5°C around 10–9 Ma (Fig. 5b). While the decreasing trend in mid-Miocene BWT is evident, the confidence intervals on the individual data points leave ambiguity on the significance of the point-to-point cooling. A Student's t-test on the bins, however, proves a significant difference in Δ_{47} between the MCO (17–14.5 Ma) and late Miocene (10–9 Ma; p=0.02; Table S1). Hence, the BWT cooling from the MCO to 9 Ma is significant. The ~8°C data point at ~8 Ma has only 23 replicates and the longest binned time interval, and because of the resulting high uncertainty we leave this data point out of our interpretations (Fig. S1). By the end of the Miocene (5 Ma), BWTs were slightly elevated (5–6 ±3°C) compared to the mid-late Miocene.

Previous studies have pointed out the unexpected warmth of mid-Miocene BWTs in their reconstructions and discussed potential but undiscernible biases on Δ_{47}-based BWT from recrystallization and pH [36–38,59]. Since benthic foraminifera at Site 1168 are well preserved (Fig. S3), and seawater chemistry, dissolution and recrystallization have very limited influence on benthic foraminifera Δ_{47} composition[60,61], we consider our BWT reconstructions reliable and confirm from Site 1168 the previous inferences of much warmer BWTs in the Miocene than present.

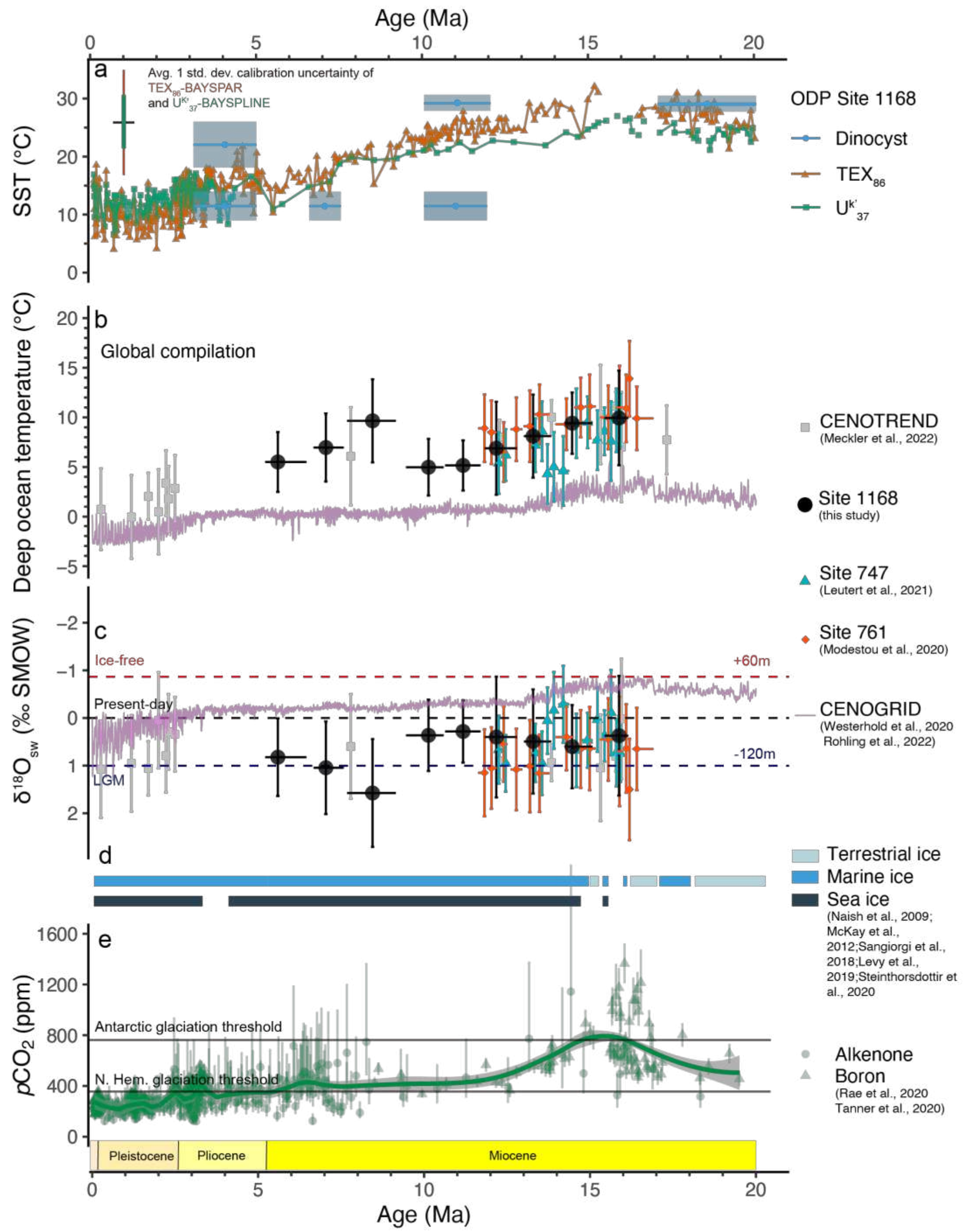

Figure 5. Compilation of records for the Neogene. (a) sea (sub)surface temperature (SST) of Site 1168 based on TEX_{86}, $U^{k'}_{37}$ [27], and dinocyst assemblages (this study). TEX_{86}, $U^{k'}_{37}$ use bayspar[62,63] and bayspline[64] calibrations, respectively. 95% confidence interval is indicated in the panel. Dinocyst-based SST estimates are based on their environmental affinities[42] in 4 time intervals (see methods). (b) Clumped isotope-based bottom water temperature (BWT) and (c) bottom water $\delta^{18}O$ ($\delta^{18}O_{sw}$) of Site 1168 along with data from Site 747[37], Site 761[36] and CENOTREND[38]. Horizontal error bars indicate the time interval of each bin. Vertical error bars indicate 95% confidence interval. Violet lines indicate the BWT and $\delta^{18}O_{sw}$ based on Rohling et al.[19] (d) Qualitative geological record of Antarctic land- and sea ice extent[21,24,33,34,65,66]. (e) pCO_2 reconstructions based on boron isotopes and alkenones $\delta^{13}C$[35,67]. Vertical error bars indicate 95% confidence interval. Solid lines

indicate the pCO_2 thresholds of glaciation based on DeConto et al.[68].

Discussion

The calculated $\delta^{18}O_{sw}$ values from Site 1168 BWTs are 0.3±0.5‰ throughout the MCO and MMCT until 9 Ma (Fig. 5c). The increase in $\delta^{18}O_{bf}$ (~1‰) from 16 to 9 Ma could in principle be all reconciled with the ~5°C BWT drop we infer from the clumped isotope data (Fig. 5b, c). Thus, our Δ_{47}-based record is different from previous far-field sea-level and deep-sea temperature syntheses based on global $\delta^{18}O$ stack[19,69], one of which recently deconvolved the mid-Miocene $\delta^{18}O_{bf}$ decline into in 2.5°C deep-sea cooling and 25 m of concurrent global average sea-level drop[19]. The discrepancy in $\delta^{18}O_{sw}$ between the study by Rohling et al.[19] and the clumped isotope data is driven by the difference in absolute BTWs and the magnitude of BWT decline. The uncertainty of the Δ_{47}-based BWT (from 9.9±4°C to 5±2.5°C) may allow for some ice volume change (0.3±0.5‰). Given the very similar MCO BWTs derived from multiple sites globally[36,37] we deem the average MCO BWT of 9.9°C reliable. By binning our MCO data with that of other sites, the uncertainty in that interval can be further reduced to ±1°C. The 5±2.5°C BWT in the 10–9 Ma interval is based on most replicates, and thus has the smallest uncertainty. Only when the 10–9 Ma BWT is at the high end of its 95% confidence interval, can the global 25m RSL (Relative Sea Level) ice volume build-up of Rohling et al.[19] be replicated with our Δ_{47} data. Given the low probability of that scenario, we conclude that the clumped isotope data imply a stronger cooling and thus less ice volume build-up during MMCT than in the model of Rohling et al.[19].

Although we have confidence in our Δ_{47}-based BWT reconstructions, the higher-than-modern $\delta^{18}O_{sw}$ for the mid-Miocene (and thus a larger than modern global ice volume) seems difficult to reconcile with evidence for Antarctic-proximal sea surface warmth[24,30], Mg/Ca-based deep-sea warmth[70] and high pCO_2 [35,71,72] during the MCO. The relatively stable long term $\delta^{18}O_{sw}$ trend (Fig. 5c) also seems hard to reconcile with major episodes of seaward Antarctic ice expansion across the MMCT, e.g., as suggested by ice-rafted debris[23,24,73]. The only scenario that reconciles all these observations is one whereby a thick AIS was situated inland at the MCO, without marine terminations[74]. Such a high, inland ice sheet would also lead to relatively low oxygen isotope ratios of Antarctic ice[75,76], because the higher-altitude ice sheet would receive less precipitation, and with a lower $\delta^{18}O$[77,78]. Thus, smaller ice volume would be needed for the mass balance if the $\delta^{18}O$ of mid-Miocene land ice was lower than previously assumed. The question is whether such a geometric change in the ice sheet with stable ice volume is dynamically plausible, under realistic boundary conditions. Understanding the detailed interactions between the ocean, climate and ice sheet involved in this situation requires extensive modelling. Here, as a first step, we test the basic viability of a significant change in the volume-to-area ratio of the Miocene Antarctic ice sheet using a stand-alone ice sheet model[78], applying a prescribed precipitation anomaly in conjunction with extreme ocean heat (Methods; Fig. 6a, b). This leads to large-scale glaciation at a ~100 ppm higher

CO_2 level than in the standard setup, yielding a thickened ice sheet interior while the build-up of ice shelves is prohibited and thereby ice area growth impeded (Fig. 6c). Furthermore, from an ice-dynamical perspective, the volume-to-area ratio of the Antarctic ice sheet waxing and waning on orbital timescales is also affected by the forcing amplitude and frequency, because the ice sheet area generally responds faster than volume to climate changes [79]. This implies that a decreased frequency or amplitude around the same mean of forcing variability could lead to an ice sheet at glacial maximum that is less extended towards the margins but thicker in the interior, and hence equally voluminous[79].

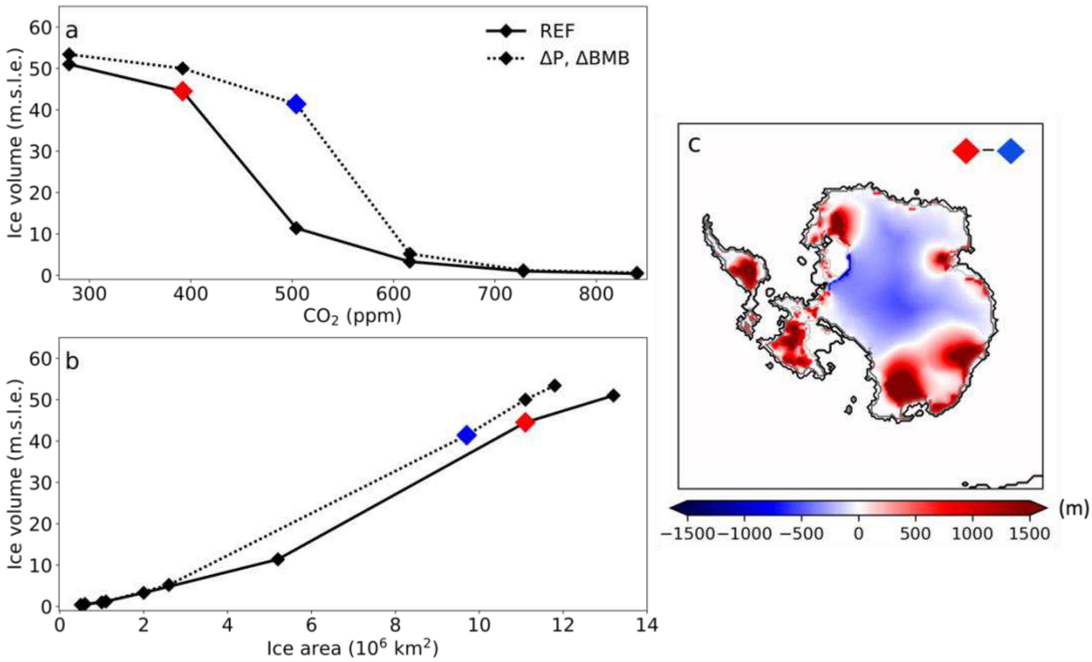

Figure 6: (a) Simulated equilibrated Antarctic ice volumes at different CO_2 levels, and (b) the relation between ice volume and ice area, yielded by a 3D thermodynamical ice sheet/shelf model (Methods). Results are obtained using the standard climate forcing (solid lines) and applying a fixed precipitation increase and extreme sub-shelf melt rates (dashed lines). (c) Equilibrated ice thickness difference between the reference simulation at 392 ppm and the simulation with anomalous forcing at 504ppm. This transition (from the blue to the red symbols) exemplifies our hypothesized Antarctic ice sheet change at the MMCT.

Following the hypothesis of a dynamic AIS geometry, then, at the MMCT the AIS increased in surface area, advanced seawards, and reduced in height (Methods; Fig. 6, switch from blue to red symbols). When the AIS undergoes spatial expansion, the periphery of the ice sheet receives a greater proportion of precipitation as compared to the central region. As a consequence of precipitation starvation in the hinterland, the overall elevation of the central AIS reduces. Such a change in geometry would have left global ice volume relatively unaltered but would have had large consequences for ice-ocean interactions and regional climate. Marine-terminating ice sheets provide profound regional cooling to have sea ice expanding[80]. The latitudinal position of westerlies and the sea ice edge determine the position of the STF[7], in absence of continental obstructions[81]. So, in principle, the gradual northwards migration of the STF that we reconstruct is in line with the abundant evidence of seawards land ice expansion across the MMCT[21,23,34]: this induced more marine-terminating ice sheets, and through that a more extensive sea ice. Also on orbital time scales, it is found that marine-terminating ice sheets were strongly sensitive to local solar insolation changes forced by obliquity[34] and so was Southern Ocean paleoceanography[82] (Fig. 5d). This local cooling of high latitudes reduced BWT and pushed ocean fronts northward.

The dinocyst assemblages, combined with previously published SST reconstructions[27] demonstrate the profound latitudinal changes of the STF. In the mid-Miocene, dinocyst assemblages were surprisingly similar between Site 1168 and the Antarctic margin[24,31,50]. Yet, perhaps counterintuitive, the latitudinal SST gradient between Australia[27] and the Ross Sea[30] was largest during MCO. This is because the south Australian Margin was ~10°C warmer than today, while the inner basins of the Ross Sea remained under local influence of the Antarctic ice sheet and thus relatively cold[30]. In any case, the strong latitudinal SST gradient testifies to the presence of ocean frontal systems that separated mid-latitude water masses from polar water masses. Our reconstructed STF migration is not without corroborating evidence. The southwards STF migration at <7 Ma is coincident with a rapid drop in radiolarian abundance at the East Tasman Plateau[58,83] and decreased K% (Potassium) in southwest Australia[84], both interpreted as a southerly shift in the frontal systems and westerlies relative to the Australian continent. At the same time, at the Agulhas Plateau[67] and in the South Atlantic[85], oceanographic reconstructions suggest an equatorward migration of oceanic fronts, rather than a southward migration as in Australia. This suggests an asymmetric behaviour of oceanic fronts around Antarctica.

With BWTs around 5°C at 7-5 Ma, we can attribute the progressive rise in $\delta^{18}O_{bf}$ of 0.2‰ between ~9 and ~6 Ma to about 20m RSL-equivalent global ice volume build-up (Fig. 5c). This is concurrent with the first significant ice accumulation in Greenland and South America[86,87] , and expansion of the west AIS[88], along with enhanced ice-rafted debris off east Antarctica[89] (Fig. 5c). The current clumped isotope data compilation (Fig. 5) points to this part of the Miocene as the phase of profound global ice volume build-up, rather than the MMCT.

The long-term Southern Ocean BWT cooling signal reconstructed from Site 1168 reflects a high-latitude surface ocean cooling, notably that of the region of deep-water formation. These surface waters where deep-water formed were arguably impacted by the seaward expansion of the ice sheet through katabatic winds[90]. This process expanded sea ice, pushing the westerlies and the STF northward (Fig. 4). In this scenario, the cooling of high latitude surface water and spatial extension of ice reduces the ocean-land thermal contrast and strengthens the polar vortex, leading to less moisture and precipitation transported into Antarctica[91,92]. The progressive cooling of subantarctic waters and increased vertical mixing induced by the northwards-migrated westerlies would have increased the efficiency of the subantarctic ocean carbon sink, the largest single ocean carbon sink system on the planet. As such, the geometric change of the ice sheet could have induced a more efficient ocean carbon storage in the subantarctic zone, which in turn contributed to the lowering of atmospheric pCO_2[93] in the Miocene (Fig. 5d).

Taken the above together, the available data show little evidence for Miocene ice volume increase forced by CO_2-induced global cooling with polar amplification[29]. First, Neogene surface ocean cooling was not amplified towards the polar regions, as the SST gradient was the largest in the warm MCO and decreasing over the mid-to-late Miocene. Second, the combined STF, BTW and deep ocean $\delta^{18}O$ reconstructions suggest that regional temperatures mostly changed due to geometric changes of the Antarctic ice sheet, rather than the other way around. Northwards expansion of sea ice and subpolar conditions occurred because of advancing marine-terminating ice sheets which induced profound regional cooling. Finally, time intervals with progressive pCO_2 decline (MMCT) seem to lack global ice volume increase, while time intervals with relatively stable pCO_2 (late Miocene) seem to have profound ice volume growth, suggesting a large role for non-linear feedbacks. These fundamental observations put a new respective on the way radiative forcing and complex feedbacks in ocean-ice-atmosphere interactions shaped Neogene ice volume and global climate trends.

Methods and Materials:

Site description

ODP Site 1168 (42°36.5809′S; 144°24.7620′E; 2463 m modern water depth) (Fig. 1) is located on the continental slope of the west-Tasmanian continental margin, with a modern seafloor temperature of 2.5°C[94]. The site sits on the northern edge of the Subtropical Convergence zone, which separates warm, saline subtropical waters from comparably cold and fresh subantarctic water masses[95]. During the Neogene, the location of Site 1168 tectonically drifted along with Tasmania and Australia from 52°S at 23 Ma to its modern position at 42°S[53]. The Neogene bathymetry was lower bathyal/upper abyssal (1000-2500m), midway on the continental slope[94]. During this northward tectonic drift, the Southern margin of Australia was continuously bathed by the eastward flowing (proto-) Leeuwin Current[40,96]. Hence, Site 1168 is well-suited to study the Neogene evolution of the STF. We applied the same age model for the sediments as in Hou et al.[27] (Fig. S4).

Palynology

We studied 131 samples for palynological content. The processing of sedimentary samples for palynological analysis followed standard procedures at the GeoLab of Utrecht University[97]. Dried sediment samples were crushed and weighed (on average 10 g, standard deviation, SD, of <1 g) before they were dissolved with 30% hydrochloric acid (HCl) and 38% hydrofluoric acid (HF) for carbonate and silicate removal, respectively. The remaining palynological residues were sieved on a 10 µm nylon mesh, using an ultrasonic bath to disintegrate agglutinated organic particles. The palynological residues were mounted on glass slides using glycerine, sealed, and counted (under 200 and 400 magnification) using an Olympus CX41 optical microscope. When possible, at least 200 dinocyst specimens were counted[98]. Samples containing less than (including) 50 dinocyst specimens were excluded for further analysis and interpretation.

We further applied the model of Thöle et al.[42] (Fig. S5) to infer paleoceanographic conditions from dinocyst assemblages. Specifically, we inferred the 25–75% SST ranges of the clusters in Thöle et al.[42] that the downcore assemblages compared most to (Fig. 2).

Foraminiferal preparation

Each sediment sample was freeze-dried, washed over a 63 µm sieve, oven-dried at 50 °C and then dry-sieved into different size fractions. We mainly picked tests of *Cibicidoides mundulus* from the 250–355 µm size fraction for our measurements. we cracked open the picked specimens and ultrasonicated the test fragments in deionized water (3*30 s) to remove adhering sediment, organic lining and nannofossils. The test fragments were dried at room temperature overnight. In order to obtain enough material, other benthic species are also processed. We use *Cibicidoides mundulus* and *Cibicidoides (Planulina) wuellerstorfi* for both stable and clumped isotopes analyses. Data from other benthic or infaunal species *Pyrgo* sp., *Gyroidina soldanii*, *Uvigerina peregerina* are only used for clumped isotopes (Fig. S2).

Clumped isotope analysis

Clumped isotope measurements were performed using Thermo Scientific MAT 253 and 253 Plus mass spectrometers at the GeoLab of Utrecht University. Both mass spectrometers were coupled to Thermo Fisher Scientific Kiel IV carbonate preparation devices. CO_2 gas was extracted from carbonate samples with phosphoric acid at a reaction temperature of 70°C. A Porapak trap included in each Kiel IV carbonate preparation system was kept at 120°C to remove organic contaminants from the sample gas. Between each run, the Porapak trap was heated at 120°C for at least 1 h for cleaning. Every measurement run included a similar number of samples and carbonate standards[99]. 3 carbonate standards (ETH-1, 2, 3) with different $\delta^{13}C$, $\delta^{18}O$ and Δ_{47} compositions and ordering states were used for monitoring and correction of the results[100]. Two additional reference standards (IAEA-C2 and Merck) were measured in each run to monitor the long-term reproducibility and stability of the instrument. We achieve the necessary precision by averaging ~30 clumped isotope values measured on small (70–100 µg) carbonate samples[100–103]. External reproducibility (1 standard deviation) in Δ47 of IAEA-C2 after correction was 0.033‰. The $\delta^{13}C$ and $\delta^{18}O$ values (reported relative to the VPDB scale) of IAEA-C2 showed an external reproducibility (1 standard deviation) of 0.18‰ and 0.21‰, respectively[104].

Deep sea temperature and $\delta^{18}O_{sw}$ calculation

We converted the sample Δ_{47} values (averages over ~30 separate measurements each) into temperature (T, in °C) using a calibration based on various recent datasets from core-top-derived foraminifera, corrected with the same carbonate standards as used in our study[105]:

$$T=\sqrt{\frac{0.0431\times10^{6}}{\Delta_{47}-0.1876}}-273.15$$

Δ47 -based BWTs were used in combination with $\delta^{18}O_{bf}$ to calculate $\delta^{18}O_{sw}$ (reported relative to VSMOW) with Eq. (9) of Marchitto et al.[106]:

$$\delta^{18}O_{bf}\,(VPDB)-\delta^{18}O_{sw}\,(VSMOW)+0.27=(-0.245\pm0.005)\times T+(0.0011\pm0.0002)\times T^{2}+(3.58\pm0.02)$$

For these calculations, $\delta^{18}O_{bf}$ values of the genus *Cibicidoides* were averaged over the same intervals as have been used for Δ_{47} averaging. Calibration uncertainties and measurement error were addressed by applying error propagation. The Meinicke et al.[105] calibration was propagated using a Matlab script that utilized a variance-covariance matrix of the slopes and intercepts, following the mathematics of the supplement of Huntington et al.[107]. It should be noted that the calibration error is very small compared to the analytical error.

Ice sheet modelling

To demonstrate the viability of a precipitation regime change leading to a fundamentally different volume-to-area ratio of the Antarctic ice sheet, we deploy the 3D thermodynamical ice sheet/shelf model IMAU-ICE v1.1.1[108]. In the standard set-up[92], climate forcing follows from pre-run warm and cold snapshot climate simulations[109]. The applied climate forcing is transiently calculated based on the prescribed CO_2 concentration and the modelled ice sheet size, through a matrix interpolation method[108]. Equilibrium experiments are performed at various CO_2 levels between preindustrial and 3x preindustrial CO_2 values, with insolation at present-day levels and initiated from an ice-free Miocene Antarctic topography[110]. Here, we perform additional sensitivity experiments, in which we apply a fixed precipitation increase and extreme sub-shelf melt rates. The precipitation anomaly is calculated as 25% of the warm snapshot precipitation fields, sub-shelf melt rates are set to 400 m/yr.

These sensitivity experiments yield large-scale glaciation at a higher CO_2 level (Fig. 6a), and an overall increased volume-to-area ratio (Fig. 6b). Notably, simultaneously reducing the CO_2 level from 504 to 394 ppm and removing the anomalous forcing, leads to significantly larger ice sheet area, while the interior ice sheet height is severely reduced (Figs. 6c, S6). These idealized experiments exemplify our hypothesized Antarctic ice sheet change at the MMCT.

Data availability:

Raw palynological counting, grouped dinocyst data, dinocyst-based SST, BWT bins and stable isotopes data are archived in Zenodo: https://doi.org/10.5281/zenodo.8146850; Clumped isotope data is archived in the EarthChem database: https://doi.org/10.26022/IEDA/112993.

References:

1. Lorenz, R. D., Lunine, J. I., Withers, P. G. & McKay, C. P. Titan, Mars and Earth : Entropy production by latitudinal heat transport. *Geophys. Res. Lett.* **28**, 415–418 (2001).
2. Barry, L., Craig, G. C. & Thuburn, J. Poleward heat transport by the atmospheric heat engine. *Nature* **415**, 774–777 (2002).
3. Holland, M. M. & Bitz, C. M. Polar amplification of climate change in coupled models. *Climate Dynamics* **21**, 221–232 (2003).
4. Toggweiler, J. R. Shifting Westerlies. *Science* **323**, 1434–1435 (2009).
5. Ferrari, R. *et al.* Antarctic sea ice control on ocean circulation in present and glacial climates. *Proceedings of the National Academy of Sciences* **111**, 8753–8758 (2014).
6. Rintoul, S. R. The global influence of localized dynamics in the Southern Ocean. *Nature* **558**, 209–218 (2018).
7. Olbers, D., Borowski, D., Völker, C. & Wölff, J.-O. The dynamical balance, transport and circulation of the Antarctic Circumpolar Current. *Antarctic Science* **16**, 439–470 (2004).
8. Toggweiler, J. R., Russell, J. L. & Carson, S. R. Midlatitude westerlies, atmospheric CO_2, and climate change during the ice ages: WESTERLIES AND CO_2 DURING THE ICE AGES. *Paleoceanography* **21**, n/a-n/a (2006).
9. Skinner, L. C., Fallon, S., Waelbroeck, C., Michel, E. & Barker, S. Ventilation of the Deep Southern Ocean and Deglacial CO_2 Rise. *Science* **328**, 1147–1151 (2010).
10. Burke, A. & Robinson, L. F. The Southern Ocean's Role in Carbon Exchange During the Last Deglaciation. *Science* **335**, 557–561 (2012).
11. Yang, H. *et al.* Tropical Expansion Driven by Poleward Advancing Midlatitude Meridional Temperature Gradients. *J. Geophys. Res. Atmos.* **125**, (2020).
12. Gaskell, D. E. *et al.* The latitudinal temperature gradient and its climate dependence as inferred from foraminiferal $\delta^{18}O$ over the past 95 million years. *Proc. Natl. Acad. Sci. U.S.A.* **119**, e2111332119 (2022).
13. Fan, T., Deser, C. & Schneider, D. P. Recent Antarctic sea ice trends in the context of Southern Ocean surface climate variations since 1950. *Geophysical Research Letters* **41**, 2419–2426 (2014).
14. Kohfeld, K. E. & Chase, Z. Temporal evolution of mechanisms controlling ocean carbon uptake during the last glacial cycle. *Earth and Planetary Science Letters* **472**, 206–215 (2017).
15. IPCC. Special Report on the Ocean and Cryosphere in a Changing Climate —. (2019).
16. DeConto, R. M. & Pollard, D. Contribution of Antarctica to past and future sea-level rise. *Nature* **531**, 591–597 (2016).
17. Baerbel Hoenisch. Paleo-CO2 data archive. (2021) doi:10.5281/ZENODO.5777278.
18. Westerhold, T. *et al.* An astronomically dated record of Earth's climate and its predictability over the last 66 million years. *Science* **369**, 1383–1387 (2020).
19. Rohling, E. J. *et al.* Comparison and Synthesis of Sea-Level and Deep-Sea Temperature Variations Over the Past 40 Million Years. *Reviews of Geophysics* **60**, (2022).
20. Herbert, T. D. *et al.* Late Miocene global cooling and the rise of modern ecosystems. *Nature Geosci*

9, 843–847 (2016).

21. Naish, T. *et al.* Obliquity-paced Pliocene West Antarctic ice sheet oscillations. *Nature* **458**, 322–328 (2009).

22. John, K. E. K. St. & Krissek, L. A. The late Miocene to Pleistocene ice-rafting history of southeast Greenland. *Boreas* **31**, 28–35 (2002).

23. Marschalek, J. W. *et al.* A large West Antarctic Ice Sheet explains early Neogene sea-level amplitude. *Nature* **600**, 450–455 (2021).

24. Sangiorgi, F. *et al.* Southern Ocean warming and Wilkes Land ice sheet retreat during the mid-Miocene. *Nat Commun* **9**, 317 (2018).

25. Herold, N., Huber, M., Müller, R. D. & Seton, M. Modeling the Miocene climatic optimum: Ocean circulation: MODELING MIOCENE OCEAN CIRCULATION. *Paleoceanography* **27**, n/a-n/a (2012).

26. Dowsett, H. *et al.* The PRISM4 (mid-Piacenzian) paleoenvironmental reconstruction. *Clim. Past* **12**, 1519–1538 (2016).

27. Hou, S. *et al.* Lipid-biomarker-based sea surface temperature record offshore Tasmania over the last 23 million years. *Climate of the Past* **19**, 787–802 (2023).

28. Zhang, Y. G., Pagani, M. & Liu, Z. A 12-Million-Year Temperature History of the Tropical Pacific Ocean. *Science* **344**, 84–87 (2014).

29. Liu, X., Huber, M., Foster, G. L., Dessler, A. & Zhang, Y. G. Persistent high latitude amplification of the Pacific Ocean over the past 10 million years. *Nat Commun* **13**, 7310 (2022).

30. Duncan, B. *et al.* Climatic and tectonic drivers of late Oligocene Antarctic ice volume. *Nat. Geosci.* **15**, 819–825 (2022).

31. Bijl, P. K. *et al.* Paleoceanography and ice sheet variability offshore Wilkes Land, Antarctica – Part 2: Insights from Oligocene–Miocene dinoflagellate cyst assemblages. *Clim. Past* **14**, 1015–1033 (2018).

32. Naish, T. R. *et al.* Sedimentary cyclicity in CRP drillcore, Victoria Land Basin, Antarctica. *Terra Antartica* **8**, 225–244 (2001).

33. Levy, R. *et al.* Antarctic ice sheet sensitivity to atmospheric CO_2 variations in the early to mid-Miocene. *Proc. Natl. Acad. Sci. U.S.A.* **113**, 3453–3458 (2016).

34. Levy, R. H. *et al.* Antarctic ice-sheet sensitivity to obliquity forcing enhanced through ocean connections. *Nature Geosci* **12**, 132–137 (2019).

35. Rae, J. W. B. *et al.* Atmospheric CO_2 over the Past 66 Million Years from Marine Archives. *Annu. Rev. Earth Planet. Sci.* **49**, 609–641 (2021).

36. Modestou, S. E., Leutert, T. J., Fernandez, A., Lear, C. H. & Meckler, A. N. Warm Middle Miocene Indian Ocean Bottom Water Temperatures: Comparison of Clumped Isotope and Mg/Ca-Based Estimates. *Paleoceanography and Paleoclimatology* **35**, (2020).

37. Leutert, T. J., Modestou, S., Bernasconi, S. M. & Meckler, A. N. Southern Ocean bottom-water cooling and ice sheet expansion during the middle Miocene climate transition. *Clim. Past* **17**, 2255–2271 (2021).

38. Meckler, A. N. *et al.* Cenozoic evolution of deep ocean temperature from clumped isotope thermometry. *Science* **377**, 86–90 (2022).

39. Sarkar, S. *et al.* Late Eocene onset of the Proto-Antarctic Circumpolar Current. *Sci Rep* **9**, 10125 (2019).

40. Hoem, F. S. *et al.* Late Eocene–early Miocene evolution of the southern Australian subtropical front: a marine palynological approach. *J. Micropalaeontol.* **40**, 175–193 (2021).

41. Evangelinos, D. *et al.* Absence of a strong, deep-reaching Antarctic Circumpolar Current zonal flow

across the Tasmanian gateway during the Oligocene to early Miocene. *Global and Planetary Change* **208**, 103718 (2022).

42. Thöle, L. *et al. An expanded database of Southern Hemisphere surface sediment dinoflagellate cyst assemblages and their oceanographic affinities*. https://eartharxiv.org/repository/view/4879/ (2023) doi:10.31223/X54948.

43. Kocken, I. J. Clumped isotope thermometry in deep time palaeoceanography.

44. Orsi, A. H., Whitworth, T. & Nowlin, W. D. On the meridional extent and fronts of the Antarctic Circumpolar Current. *Deep Sea Research Part I: Oceanographic Research Papers* **42**, 641–673 (1995).

45. Torsvik, T. H. *et al.* Phanerozoic polar wander, palaeogeography and dynamics. *Earth-Science Reviews* **114**, 325–368 (2012).

46. Gersonde, R. *et al.* Last glacial sea surface temperatures and sea-ice extent in the Southern Ocean (Atlantic-Indian sector): A multiproxy approach. *Paleoceanography* **18**, (2003).

47. Bostock, H. C., Hayward, B. W., Neil, H. L., Sabaa, A. T. & Scott, G. H. Changes in the position of the Subtropical Front south of New Zealand since the last glacial period: STF AROUND NEW ZEALAND. *Paleoceanography* **30**, 824–844 (2015).

48. Gray, W. R. *et al.* Poleward shift in the Southern Hemisphere westerly winds synchronous with the deglacial rise in CO2. (2021).

49. Bijl, P., Boterblom, W. H., Sangiorgi, F., Hartman, J. D. & Peterse, F. Oligocene-Miocene paleoceanographic changes offshore the Wilkes Land Margin, Antarctica: dinoflagellate cyst and TEX86 analyses of DSDP Site 269. 11932 (2017).

50. Warny, S. *et al.* Palynomorphs from a sediment core reveal a sudden remarkably warm Antarctica during the middle Miocene. *Geology* **37**, 955–958 (2009).

51. Grant, G. R. *et al.* Amplified surface warming in the Southwest Pacific during the mid-Pliocene (3.3–3.0 Ma) and future implications. *EGUsphere* 1–33 (2023) doi:10.5194/egusphere-2023-108.

52. Müller, R. D. *et al.* GPlates: Building a Virtual Earth Through Deep Time. *Geochemistry, Geophysics, Geosystems* **19**, 2243–2261 (2018).

53. van Hinsbergen, D. J. J. *et al.* A Paleolatitude Calculator for Paleoclimate Studies. *PLOS ONE* **10**, e0126946 (2015).

54. Holbourn, A., Kuhnt, W., Clemens, S., Prell, W. & Andersen, N. Middle to late Miocene stepwise climate cooling: Evidence from a high-resolution deep water isotope curve spanning 8 million years: MIOCENE BENTHIC ISOTOPES. *Paleoceanography* **28**, 688–699 (2013).

55. Holbourn, A., Kuhnt, W., Schulz, M., Flores, J.-A. & Andersen, N. Orbitally-paced climate evolution during the middle Miocene "Monterey" carbon-isotope excursion. *Earth and Planetary Science Letters* **261**, 534–550 (2007).

56. Holbourn, A., Kuhnt, W., Kochhann, K. G. D., Andersen, N. & Sebastian Meier, K. J. Global perturbation of the carbon cycle at the onset of the Miocene Climatic Optimum. *Geology* **43**, 123–126 (2015).

57. Kochhann, K. G. D. *et al.* Eccentricity pacing of eastern equatorial Pacific carbonate dissolution cycles during the Miocene Climatic Optimum. *Paleoceanography* **31**, 1176–1192 (2016).

58. Diester-Haass, L., Billups, K. & Emeis, K. C. Late Miocene carbon isotope records and marine biological productivity: Was there a (dusty) link? *Paleoceanography* **21**, (2006).

59. Agterhuis, T., Ziegler, M., de Winter, N. J. & Lourens, L. J. Warm deep-sea temperatures across Eocene Thermal Maximum 2 from clumped isotope thermometry. *Commun Earth Environ* **3**, 39 (2022).

60. Leutert, T. J. *et al.* Sensitivity of clumped isotope temperatures in fossil benthic and planktic

foraminifera to diagenetic alteration. *Geochimica et Cosmochimica Acta* **257**, 354–372 (2019).
61. Edgar, K. M., Hull, P. M. & Ezard, T. H. G. Evolutionary history biases inferences of ecology and environment from δ13C but not δ18O values. *Nat Commun* **8**, 1106 (2017).
62. Tierney, J. E. & Tingley, M. P. A Bayesian, spatially-varying calibration model for the TEX86 proxy. *Geochimica et Cosmochimica Acta* **127**, 83–106 (2014).
63. Tierney, J. E. & Tingley, M. P. A TEX86 surface sediment database and extended Bayesian calibration. *Sci Data* **2**, 150029 (2015).
64. Tierney, J. E. & Tingley, M. P. BAYSPLINE: A New Calibration for the Alkenone Paleothermometer. *Paleoceanography and Paleoclimatology* **33**, 281–301 (2018).
65. McKay, R. *et al.* Antarctic and Southern Ocean influences on Late Pliocene global cooling. *Proc. Natl. Acad. Sci. U.S.A.* **109**, 6423–6428 (2012).
66. Steinthorsdottir, M. *et al.* The Miocene: The Future of the Past. *Paleoceanogr Paleoclimatol* **36**, (2021).
67. Tanner, T., Hernández-Almeida, I., Drury, A. J., Guitián, J. & Stoll, H. Decreasing Atmospheric CO_2 During the Late Miocene Cooling. *Paleoceanography and Paleoclimatology* **35**, (2020).
68. DeConto, R. M. *et al.* Thresholds for Cenozoic bipolar glaciation. *Nature* **455**, 652–656 (2008).
69. Boer, B. D., Wal, R. S. W. van de, Bintanja, R., Lourens, L. J. & Tuenter, E. Cenozoic global ice-volume and temperature simulations with 1-D ice-sheet models forced by benthic δ18O records. *Annals of Glaciology* **51**, 23–33 (2010).
70. Lear, C. H. *et al.* Neogene ice volume and ocean temperatures: Insights from infaunal foraminiferal Mg/Ca paleothermometry. *Paleoceanography* **30**, 1437–1454 (2015).
71. Sosdian, S. M. *et al.* Constraining the evolution of Neogene ocean carbonate chemistry using the boron isotope pH proxy. *Earth and Planetary Science Letters* **498**, 362–376 (2018).
72. Super, J. R. *et al.* North Atlantic temperature and pCO2 coupling in the early-middle Miocene. *Geology* **46**, 519–522 (2018).
73. Pierce, E. L. *et al.* Evidence for a dynamic East Antarctic ice sheet during the mid-Miocene climate transition. *Earth and Planetary Science Letters* **478**, 1–13 (2017).
74. Passchier, S. *et al.* Early and middle Miocene Antarctic glacial history from the sedimentary facies distribution in the AND-2A drill hole, Ross Sea, Antarctica. *Geological Society of America Bulletin* **123**, 2352–2365 (2011).
75. Goursaud, S. *et al.* Challenges associated with the climatic interpretation of water stable isotope records from a highly resolved firn core from Adélie Land, coastal Antarctica. *The Cryosphere* **13**, 1297–1324 (2019).
76. Langebroek, P. M., Paul, A. & Schulz, M. Simulating the sea level imprint on marine oxygen isotope records during the middle Miocene using an ice sheet-climate model: MODELING OXYGEN ISOTOPES IN THE MIOCENE. *Paleoceanography* **25**, n/a-n/a (2010).
77. Gasson, E., DeConto, R. M. & Pollard, D. Modeling the oxygen isotope composition of the Antarctic ice sheet and its significance to Pliocene sea level. *Geology* **44**, 827–830 (2016).
78. Stap, L. B., Sutter, J., Knorr, G., Stärz, M. & Lohmann, G. Transient Variability of the Miocene Antarctic Ice Sheet Smaller Than Equilibrium Differences. *Geophysical Research Letters* **46**, 4288–4298 (2019).
79. Stap, L. B., Berends, C. J. & van de Wal, R. S. W. Miocene Antarctic ice sheet area responds significantly faster than volume to CO_2-induced climate change. *Climate of the Past Discussions* 1–19 (2023) doi:10.5194/cp-2023-12.

80. DeConto, R., Pollard, D. & Harwood, D. Sea ice feedback and Cenozoic evolution of Antarctic climate and ice sheets. *Paleoceanography* **22**, (2007).

81. Hill, D. J. *et al.* Paleogeographic controls on the onset of the Antarctic circumpolar current. *Geophysical Research Letters* **40**, 5199–5204 (2013).

82. Salabarnada, A. *et al.* Paleoceanography and ice sheet variability offshore Wilkes Land, Antarctica – Part 1: Insights from late Oligocene astronomically paced contourite sedimentation. *Clim. Past* **14**, 991–1014 (2018).

83. Christensen, B. A. *et al.* Late Miocene Onset of Tasman Leakage and Southern Hemisphere Supergyre Ushers in Near-Modern Circulation. *Geophysical Research Letters* **48**, (2021).

84. Groeneveld, J. *et al.* Australian shelf sediments reveal shifts in Miocene Southern Hemisphere westerlies. *Sci. Adv.* **3**, e1602567 (2017).

85. Kato, Y. Diatom-based reconstruction of the Subantarctic Front migrations during the late Miocene and Pliocene. *Marine Micropaleontology* **160**, 101908 (2020).

86. Larsen, H. C. *et al.* Seven Million Years of Glaciation in Greenland. *Science* **264**, 952–955 (1994).

87. Mercer, J. H. & Sutter, J. F. Late miocene—earliest pliocene glaciation in southern Argentina: implications for global ice-sheet history. *Palaeogeography, Palaeoclimatology, Palaeoecology* **38**, 185–206 (1982).

88. *LATEST CRETACEOUS TO CENOZOIC CLIMATE AND OCEANOGRAPHIC DEVELOPMENTS IN THE WEDDELL SEA, ANTARCTICA: AN OCEAN-DRILLING PERSPECTIVE*. vol. 113 (Ocean Drilling Program, 1990).

89. Williams, T. *et al.* Evidence for iceberg armadas from East Antarctica in the Southern Ocean during the late Miocene and early Pliocene. *Earth and Planetary Science Letters* **290**, 351–361 (2010).

90. Bradshaw, C. D. *et al.* Hydrological impact of Middle Miocene Antarctic ice-free areas coupled to deep ocean temperatures. *Nat. Geosci.* **14**, 429–436 (2021).

91. Naakka, T., Nygård, T. & Vihma, T. Air Moisture Climatology and Related Physical Processes in the Antarctic on the Basis of ERA5 Reanalysis. *Journal of Climate* **34**, 4463–4480 (2021).

92. Stap, L. B., Berends, C. J., Scherrenberg, M. D. W., van de Wal, R. S. W. & Gasson, E. G. W. Net effect of ice-sheet–atmosphere interactions reduces simulated transient Miocene Antarctic ice-sheet variability. *The Cryosphere* **16**, 1315–1332 (2022).

93. Herbert, T. D. *et al.* Tectonic degassing drove global temperature trends since 20 Ma. *Science* **377**, 116–119 (2022).

94. Exon, N. F., Kennett, J. P. & Malone, M. J. *Ocean Drilling Program Leg 189 Initial Reports: Chapter 3*. (2001).

95. Stickley, C. E. *et al. Proceedings of the Ocean Drilling Program, 189 Scientific Results*. vol. 189 (Ocean Drilling Program, 2004).

96. McGowran, B., Holdgate, G. R., Li, Q. & Gallagher, S. J. Cenozoic stratigraphic succession in southeastern Australia. *Aust J Earth Sci* **51**, 459–496 (2004).

97. Brinkhuis, H. *et al. LATE EOCENE–QUATERNARY DINOFLAGELLATE CYSTS FROM ODP SITE 1168, OFF WESTERN TASMANIA*. vol. 189 (Ocean Drilling Program, 2004).

98. Mertens, K. N. *et al.* Determining the absolute abundance of dinoflagellate cysts in recent marine sediments: The Lycopodium marker-grain method put to the test. *Review of Palaeobotany and Palynology* **157**, 238–252 (2009).

99. Kocken, I. J., Müller, I. A. & Ziegler, M. Optimizing the Use of Carbonate Standards to Minimize Uncertainties in Clumped Isotope Data. *Geochemistry, Geophysics, Geosystems* **20**, 5565–5577 (2019).

100. Bernasconi, S. M. *et al.* InterCarb: A Community Effort to Improve Interlaboratory Standardization of the Carbonate Clumped Isotope Thermometer Using Carbonate Standards. *Geochem Geophys Geosyst* **22**, (2021).
101. Hu, B. *et al.* A modified procedure for gas-source isotope ratio mass spectrometry: the long-integration dual-inlet (LIDI) methodology and implications for clumped isotope measurements. *Rapid Communications in Mass Spectrometry* **28**, 1413–1425 (2014).
102. Meckler, A. N., Ziegler, M., Millán, M. I., Breitenbach, S. F. M. & Bernasconi, S. M. Long-term performance of the Kiel carbonate device with a new correction scheme for clumped isotope measurements. *Rapid Communications in Mass Spectrometry* **28**, 1705–1715 (2014).
103. Bernasconi, S. M. *et al.* Reducing Uncertainties in Carbonate Clumped Isotope Analysis Through Consistent Carbonate-Based Standardization. *Geochemistry, Geophysics, Geosystems* **19**, 2895–2914 (2018).
104. Hou, S., Ziegler, M., Paul, R. & Bijl, P. K. Clumped isotope-based bottom water temperature record west off-shore Tasmania from 16 to 5 Ma. Interdisciplinary Earth Data Alliance (IEDA). https://doi.org/10.26022/IEDA/112993. (2023). Accessed 2023-07-18.
105. Meinicke, N. *et al.* A robust calibration of the clumped isotopes to temperature relationship for foraminifers. *Geochimica et Cosmochimica Acta* **270**, 160–183 (2020).
106. Marchitto, T. M. *et al.* Improved oxygen isotope temperature calibrations for cosmopolitan benthic foraminifera. *Geochimica et Cosmochimica Acta* **130**, 1–11 (2014).
107. Huntington, K. W. *et al.* Methods and limitations of 'clumped' CO2 isotope (Δ47) analysis by gas-source isotope ratio mass spectrometry. *Journal of Mass Spectrometry* **44**, 1318–1329 (2009).
108. Berends, C. J., de Boer, B. & van de Wal, R. S. W. Application of HadCM3@Bristolv1.0 simulations of paleoclimate as forcing for an ice-sheet model, ANICE2.1: set-up and benchmark experiments. *Geoscientific Model Development* **11**, 4657–4675 (2018).
109. Burls, N. J. *et al.* Simulating Miocene Warmth: Insights From an Opportunistic Multi-Model Ensemble (MioMIP1). *Paleoceanogr Paleoclimatol* **36**, (2021).
110. Paxman, G. J. G. *et al.* Reconstructions of Antarctic topography since the Eocene–Oligocene boundary. *Palaeogeography, Palaeoclimatology, Palaeoecology* **535**, 109346 (2019).

Acknowledgements:

We thank Mariska Hoorweg, Natasja Welters, Giovanni Dammers, Desmond Eefting and Arnold van Dijk for laboratory assistance. We thank IODP and scientists of ODP Leg 189, and technicians at KCC in Kochi, Japan for the help with sampling. We are grateful to Tobias Agterhuis, Ilja Kocken and Elena Dominguez Valdes for insightful discussion regarding clumped isotopes. This research is funded by ERC Starting Grant 802835 to Peter K. Bijl.

Author contributions:

PKB designed the research. SH, MN and FSH processed and analyzed samples for palynology. SH, RP and AS generated the stable isotopes data. SH and RP washed the foraminifera samples and generated the clumped isotope data. LBS performed the ice sheet modelling. SH wrote the paper with input from

PKB, AS, MZ and FS.

Competing interests:

The authors declare no competing interests.

Supplementary Files

This is a list of supplementary files associated with this preprint. Click to download.

- NCHouetalsupplementaryfinal.pdf